



RESEARCH LETTER

10.1002/2017GL073419

Key Points:

- First direct confirmation of correlation between lunar surface photoelectron flux and solar photon flux
- Develops an observation-based model of emitted photoelectron energy spectra from lunar soil
- Dayside lunar surface potentials in the Earth's tail lobes could increase by a factor of 2–3 during strong solar flares

Correspondence to:

Y. Harada,
haraday@ssl.berkeley.edu

Citation:

Harada, Y., A. R. Poppe, J. S. Halekas, P. C. Chamberlin, and J. P. McFadden (2017), Photoemission and electrostatic potentials on the dayside lunar surface in the terrestrial magnetotail lobes, *Geophys. Res. Lett.*, *44*, doi:10.1002/2017GL073419.

Received 10 MAR 2017

Accepted 23 MAY 2017

Accepted article online 30 MAY 2017

Photoemission and electrostatic potentials on the dayside lunar surface in the terrestrial magnetotail lobes

Y. Harada^{1,2} , A. R. Poppe¹ , J. S. Halekas² , P. C. Chamberlin³ , and J. P. McFadden¹

¹Space Sciences Laboratory, University of California, Berkeley, California, USA, ²Department of Physics and Astronomy, University of Iowa, Iowa City, Iowa, USA, ³NASA Goddard Space Flight Center, Greenbelt, Maryland, USA

Abstract Despite the need to accurately predict and assess the lunar electrostatic environment in all ambient conditions that the Moon encounters, photoemission and electrostatic potentials on the dayside lunar surface in the terrestrial magnetotail lobes remain poorly characterized. We study characteristics and variabilities of lunar photoelectron energy spectra by utilizing Acceleration, Reconnection, Turbulence, and Electrodynamics of the Moon's Interaction with the Sun (ARTEMIS) and Apollo measurements in combination with the Flare Irradiance Spectral Model (FISM). We confirm that the photoelectron spectral shapes are consistent between ARTEMIS and Apollo and that the photoelectron flux is linearly correlated with the FISM solar photon flux. We develop an observation-based model of lunar photoelectron energy distributions, thereby deriving the current balance surface potential. The model predicts that dayside lunar surface potentials in the tail lobes (typically tens of volts) could increase by a factor of 2–3 during strong solar flares.

1. Introduction

The dayside lunar surface is constantly bombarded by solar photons and ambient charged particles, inducing a variety of surface processes (e.g., photoemission, secondary electron emission, sputtering, photon- and electron-induced desorption, and absorption and implantation of bombarding particles). The resulting charge transfer between the lunar surface and space causes surface charging such that electric currents into and out of the surface are balanced [e.g., Manka, 1973]. The dominant currents on the sunlit lunar surface are provided by the incoming ambient electrons and photoelectrons escaping from a positive potential sheath formed above the surface. The escaping photoelectron flux is derived by integrating the energy distribution of photoelectrons that overcome the positive potential barrier. Photoelectron energy distributions generally exhibit two components under solar irradiation: (i) a cold core population with a mean energy of ~ 1 – 2 eV and (ii) a slowly decreasing high-energy tail at $> \sim 10$ eV [Whipple, 1981; Pedersen, 1995]. In a low-density plasma regime, such as in the terrestrial magnetotail lobes, the incoming electron flux becomes so small that the surface charges up to large potentials in order to prevent the high-energy photoelectrons from escaping, as is evident from observations of lunar pickup ions with nonzero parallel velocities [Tanaka et al., 2009; Poppe et al., 2012a; Harada et al., 2013]. Strong surface charging potentially causes dynamic charged dust transport [Stubbs et al., 2006; Sternovsky et al., 2008] and modifies exospheric pickup ion dynamics [Poppe et al., 2013]. In order to assess lunar surface charging for a variety of plasma and solar conditions, we must characterize the energy distribution of lunar surface photoelectrons over a wide range of energies from ~ 1 eV to hundreds of eV.

In situ measurements of lunar surface photoelectrons are classified into two types: measurements (i) on the lunar surface and (ii) from orbiting spacecraft. As illustrated in Figure 1, the cold photoelectrons with energies lower than $|eU_M|$, where e is the electron charge and U_M is the lunar surface potential with respect to the ambient plasma, are attracted back to the surface by the positively charged lunar surface. Electron instruments with upward looking apertures installed on the lunar surface (such as those deployed by the Apollo missions) can detect these trapped photoelectrons. Meanwhile, photoelectrons with energies higher than $|eU_M|$ escape from the lunar surface potential barrier and travel upward along the magnetic field. These escaping photoelectrons can be measured by spacecraft on field lines connected to the lunar surface.

Lunar photoelectron measurements on the surface were conducted by the Charged Particle Lunar Environment (CPLEE) instrument at the Apollo 14 site [Reasoner and Burke, 1973] and by the Solar Wind Spectrometer

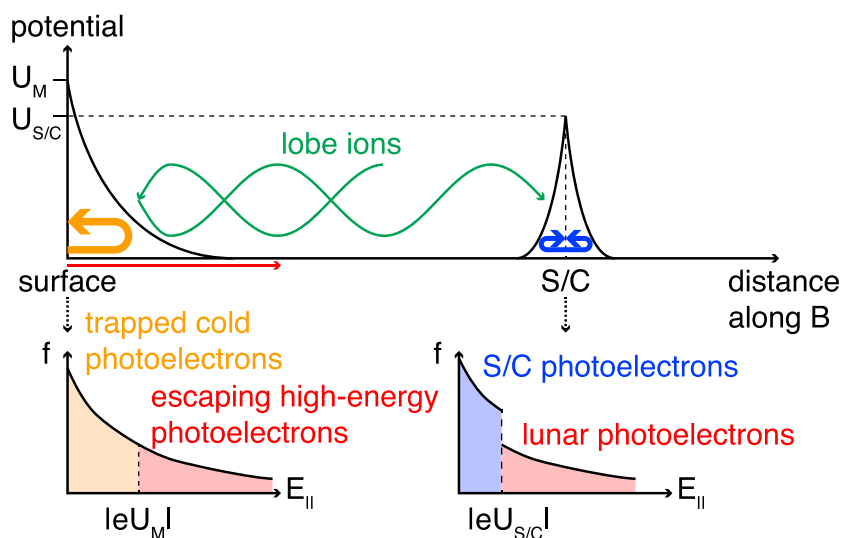


Figure 1. Schematic illustration of electrostatic potential profile along the magnetic field line above the dayside lunar surface and photoelectron energy distributions on the surface and at the spacecraft.

(SWS) at the Apollo 12 and 15 sites [Goldstein, 1974]. Reasoner and Burke [1973] presented CPLEE measurements of lunar photoelectrons with energies between 40 and 200 eV and showed that the photoelectron energy spectra follow a power law distribution, $J(E) \propto E^{-k}$, with $3.5 < k < 4$. The measured count rate diminished as the Moon entered eclipse, suggesting that solar photons are the predominant driver of the electron emission. SWS measurements of 5–40 eV electrons show that the power law spectrum extends to the lower energy range below 40 eV [Goldstein, 1974]. The CPLEE observations of the trapped photoelectrons with energies up to 200 eV suggested the presence of unexpectedly large positive potentials on the dayside lunar surface in the Earth’s magnetotail, +80 V in the plasma sheet and over +200 V in the tail lobes, which are much higher than the equilibrium potentials predicted from the current balance solution [Burke et al., 1975]. Burke et al. [1975] attributed the discrepancy to an additional potential generated by charge separation of heavier ions and lighter electrons above the magnetized surface (the crustal magnetic field strength is estimated to be ~ 75 nT at the CPLEE site).

This paper presents spacecraft measurements of escaping lunar photoelectrons based on plasma and field data obtained by the Acceleration, Reconnection, Turbulence, and Electrodynamics of the Moon’s Interaction with the Sun (ARTEMIS) mission [Angelopoulos, 2011]. ARTEMIS observed clear signatures of photoelectrons emitted from the dayside lunar surface when the Moon was located in the terrestrial magnetotail lobes [Harada et al., 2013]. We note that the CPLEE measurements of trapped lunar photoelectrons on the surface could be contaminated by photoelectrons emitted from the instrument surfaces (although the instrumental photoelectron contribution was estimated to be small [Reasoner and Burke, 1973]). In contrast, with the spacecraft potential information directly measured by ARTEMIS, lunar photoelectrons can be cleanly separated from the spacecraft/instrumental photoelectrons (Figure 1). Based on the ARTEMIS and Apollo measurements and solar photon flux provided by the Flare Irradiance Spectral Model (FISM) [Chamberlin et al., 2007, 2008], we develop an empirical model of the lunar photoelectron energy spectrum accounting for solar flux variations. We utilize the model photoelectron spectrum to predict positive potentials on the unmagnetized regions of the sunlit lunar surface in the terrestrial magnetotail lobes.

2. ARTEMIS Observations of Photoemission and Potentials on the Dayside Unmagnetized Lunar Surface in the Earth’s Tail Lobes

2.1. A Case Study

Figure 2 shows an example of ARTEMIS observations above the dayside lunar surface in the terrestrial magnetotail lobes. We observe cold lobe ions at ~ 10 –200 eV (Figure 2a), warm electrons below ~ 400 eV, (Figure 2b), and stable, B_x -dominant magnetic fields (Figure 2d). The distance along the magnetic field line from the spacecraft to the lunar surface, estimated from straight line tracing, was $\sim 0.3 R_L$ (Figure 2e), where R_L is the lunar

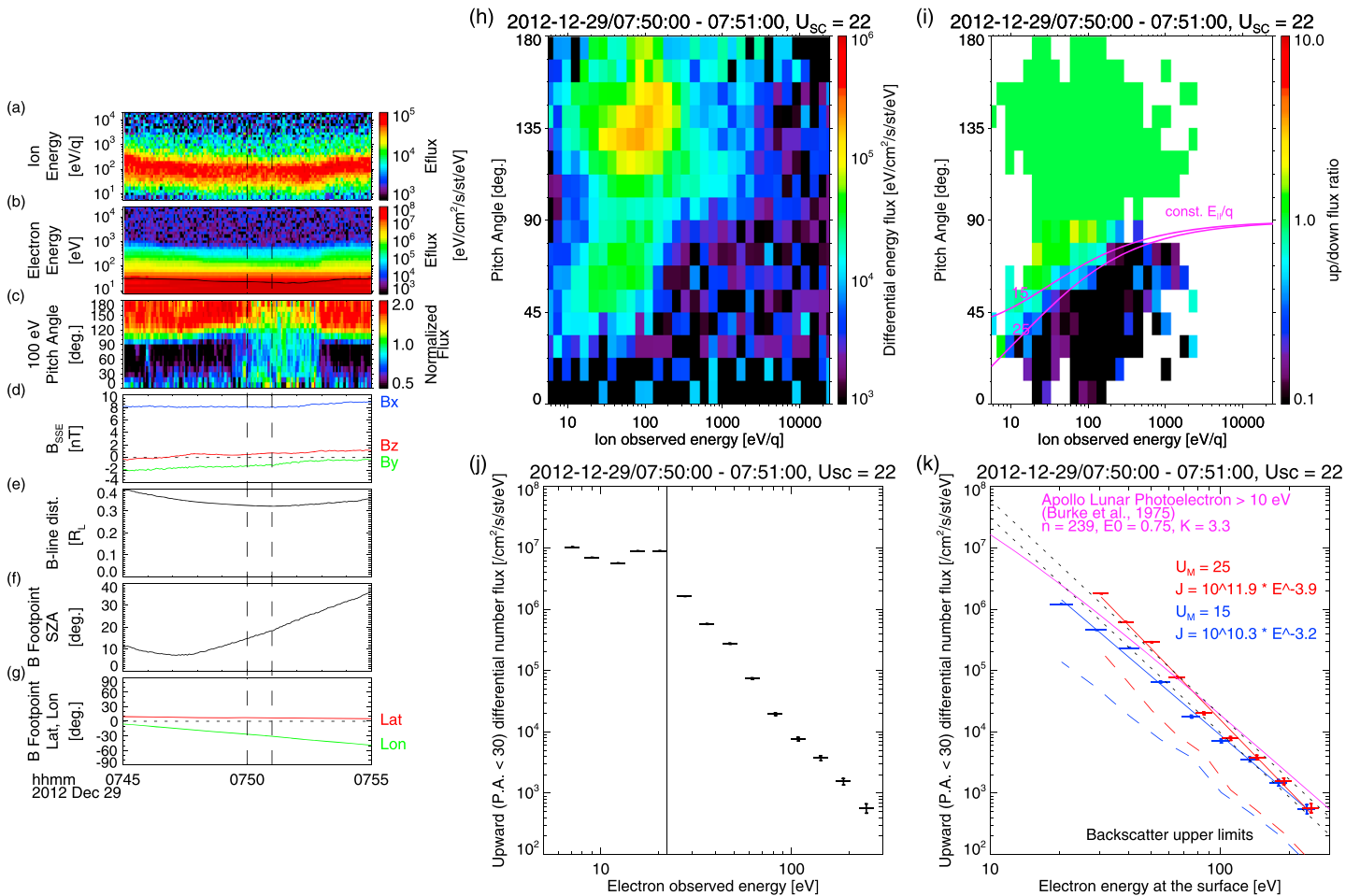


Figure 2. ARTEMIS P1 observations above the dayside lunar surface when the Moon was located in the northern lobe of the terrestrial magnetotail at 07:45–07:55 UT on 29 December 2012. Time series of energy spectra of (a) ions and (b) electrons, (c) pitch angle distributions of 100 eV electrons measured by ESA [McFadden et al., 2008], (d) magnetic fields in the selenocentric solar ecliptic (SSE) coordinates measured by FGM [Auster et al., 2008], (e) magnetic field line distances from the spacecraft to the lunar surface, (f) solar zenith angles of the field line foot point, and (g) latitudes and longitudes of the foot point. The black line in Figure 2b represents the spacecraft potential measured by EFI [Bonnell et al., 2008]. One minute averages between 07:50 and 07:51 UT (indicated by the dashed lines in Figures 2a–2g) of ion energy-pitch angle distributions in units of (h) differential energy flux and (i) upward/downward flux ratio, and energy spectra of parallel electrons (pitch angles <math><30^\circ</math>) with (j) observed energies and (k) electron energies at the lunar surface (see text for detail).

radius ($R_L = 1738$ km). The field line foot point was located at the near-subsolar region with low solar zenith angles $<30^\circ$ (Figure 2f) and at selenographic longitudes of $0\text{--}50^\circ\text{W}$ and latitudes of $\sim 5^\circ\text{N}$ (Figure 2g), where only very weak crustal magnetic fields (<10 nT at the surface) are present [Halekas et al., 2001; Mitchell et al., 2008; Tsunakawa et al., 2015]. The pitch angle distributions of 100 eV electrons (Figure 2c) show the downward traveling lobe electrons with pitch angles of $90\text{--}180^\circ$ (which could be modified by the interaction with local cold plasma of lunar origin [Harada et al., 2013]) and upward traveling, parallel electrons with lower fluxes. During this time period, we do not observe adiabatically reflected electrons at $0\text{--}90^\circ$ pitch angles, which should have fluxes comparable to the incident electron fluxes [e.g., Mitchell et al., 2008]. The absence of magnetically reflected lobe electrons is consistent with field line connection to the mostly unmagnetized surface.

In the absence of crustal magnetic fields, cold lobe ions incident on the positively charged lunar surface will be electrostatically reflected, as illustrated in Figure 1, if $E_{\parallel} < qU_M$, where E_{\parallel} is the energy parallel to the magnetic field and q is the charge of lobe ions. We note that the gyroradii of these lobe ions (~ 120 km for 50 eV protons in a 8 nT magnetic field) are much smaller than the lunar radius, allowing one-dimensional treatment of ion motion along the magnetic field above the near-subsolar surface. Some of the reflected ions can be detected by ARTEMIS, if the ions have sufficiently high total energies, $E = E_{\parallel} + E_{\perp}$, to overcome the spacecraft potential U_{SC} . Note that the ion gyroradii are much larger than the spatial size of the spacecraft (~ 1 m). Figure 2h shows the ion energy-pitch angle distributions taken at 07:50–07:51 UT (indicated by the

dashed lines in Figures 2a–2g). In addition to the downward traveling lobe ions with pitch angles $\alpha > 90^\circ$, we observe the upward traveling ions ($\alpha < 90^\circ$) with fluxes comparable to those at the corresponding energy-pitch angle bins ($180^\circ - \alpha$) on the downward side. This is clearly seen in the upward/downward flux ratio distribution shown in Figure 2i. The magenta lines in Figures 2i denote the contours of E_{\parallel}/q of 15 eV/q and 25 eV/q, where $E_{\parallel}/q = E/q \cdot \cos^2 \alpha = (E_{\text{obs}}/q + U_{\text{SC}}) \cos^2 \alpha$. We can expect the flux ratio to be unity for the reflected ions with $E_{\parallel}/q < U_M$ and nearly zero for the ions striking the lunar surface with $E_{\parallel}/q > U_M$. Figure 2i exhibits flux ratios $r \sim 1$ at $E_{\parallel}/q < 15$ eV/q, $0 < r < 1$ between 15 eV/q $< E_{\parallel}/q < 25$ eV/q and $r \sim 0$ at $E_{\parallel}/q > 25$ eV/q. This ion reflectometry method constrains U_M to be between +15 V and +25 V. We note that the ion reflection magnetometry was developed to probe surface magnetic field strengths at Mercury [Winslow *et al.*, 2014], whereas we utilize electrostatic ion reflection to probe potentials on the unmagnetized surfaces of the Moon.

Figure 2j shows the measured energy spectrum of the upward traveling, parallel electrons with pitch angles $< 30^\circ$ at 07:50–07:51 UT. The vertical line marks the measured spacecraft potential, which clearly separates the ambient electrons (above $|eU_{\text{SC}}|$) from the spacecraft photoelectron contamination (below $|eU_{\text{SC}}|$). Figure 2k shows the energy spectra of upward electrons emitted from the lunar surface corrected for U_{SC} and U_M , where U_M is taken from the upper and lower limits constrained by the ion measurements. The measured electron flux at 20–300 eV is well above the upper limit of the estimated backscatter flux indicated by the dashed, red and blue lines (10% of the downward electron flux [Lin and Gopalan, 1991]), suggesting that these electrons consist mostly of photoelectrons emitted from the lunar surface. Each electron spectrum is approximately power law in shape, as demonstrated by straight line fitting in the log-log plot with a spectral index k between 3 and 4. The shape of the photoelectron energy spectrum measured by ARTEMIS is consistent with the Apollo measurements of > 10 eV lunar photoelectrons indicated by the magenta line (a kappa function [Vasyliunas, 1968] with parameters of $N = 239 \text{ cm}^{-3}$, $E_0 = 0.75$ eV, and $\kappa = 3.3$ taken from Figure 2 of Burke *et al.* [1975]).

2.2. Statistical Results

We examine the variability of the lunar photoelectron energy spectra utilizing long-term data obtained by the two ARTEMIS probes from July 2011 to September 2016. As the flux of photoemitted electrons induced by energetic photons should be proportional to the incident photon flux, the lunar photoelectron spectra are expected to exhibit variations associated with solar photon flux variations. In order to develop a statistical data set of clean energy spectra of photoelectrons emitted from the unmagnetized region of the near-subsolar lunar surface, we selected time intervals based on the following criteria: (i) the Moon is located within $\pm 30^\circ$ from the Earth-anti-Sun line; (ii) the 100–10,000 eV downward electron flux is below $5 \times 10^6 \text{ /cm}^2/\text{s}$; (iii) the electron beta is lower than 0.05; (iv) the spacecraft potential is lower than +40 V; (v) the distance along the field line from the spacecraft to the lunar surface is below $1 R_L$; (vi) the solar zenith angle of the field line foot point is smaller than 30° ; (vii) the foot point latitude is between 0 and 30° N ; and (viii) the foot point longitude is between 50° W and 10° W . The criteria (i)–(iii) are imposed to select intervals when the Moon was located in the terrestrial magnetotail lobes and the lunar surface is exposed to relatively low fluxes of hot electrons, in which case contamination from backscattered and electron-induced secondary electrons is negligible. We chose the spacecraft potential threshold (iv) so that we can obtain a wide band of energy spectra with good counting statistics uncontaminated by spacecraft photoelectrons. The field line geometry conditions (v)–(viii) restrict the spacecraft location to low altitudes and the foot point location to near-subsolar regions and surface areas with weak or no crustal magnetic fields [Halekas *et al.*, 2001; Mitchell *et al.*, 2008; Tsunakawa *et al.*, 2015].

Figure 3a shows the collection of 829 energy spectra of upward traveling electrons obtained during the selected intervals. Since the U_M information estimated by the ion reflectometry described in section 2.1 is not always available (because measurable cold lobe ions are often absent), Figure 3a shows the upward electron flux as a function of observed energy, instead of electron energy at the surface. If $U_M \sim U_{\text{SC}}$, which is the case for the 29 December 2012 event shown in Figure 2, the observed energies are roughly equal to the energies at the surface. We note that the uncertainty of $U_M - U_{\text{SC}}$ (probably $< \sim 10$ V, based on the 29 December 2012 event) would have minimal effects on photoelectron energy spectra at higher energies $> \sim 100$ eV. The colors indicate the flux of 1–5 nm (247–1239 eV) solar photons obtained from 60 s resolution FISM spectra [Chamberlin *et al.*, 2008]. For monochromatic X-ray photons (0.1–10 keV) incident on a solid, photoemitted fast (> 50 eV) electrons consist of sharp lines of elastically scattered primary photoelectrons and Auger electrons and a much larger number of their low-energy tails of inelastically scattered primaries [Henke *et al.*, 1977, 1981]. Since most of the fast photoelectrons are emitted with energies slightly lower than the incident photon energies,

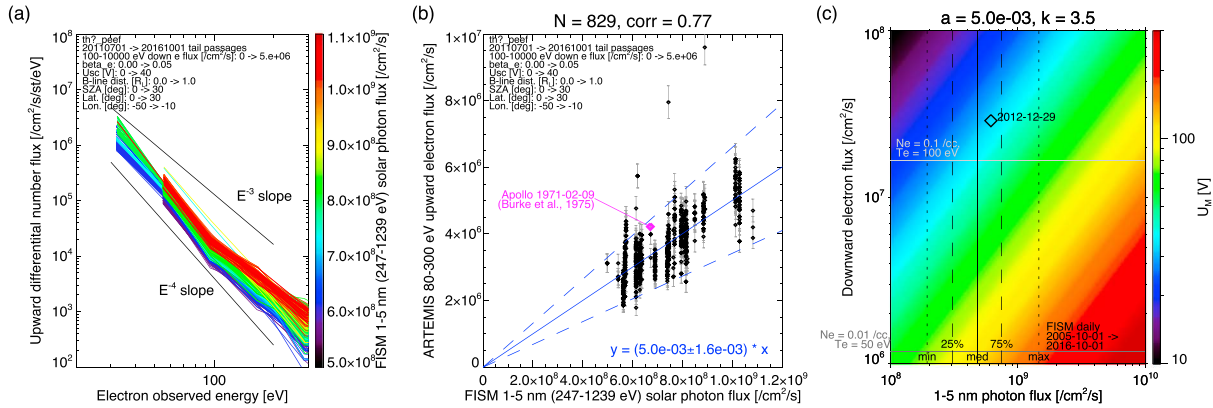


Figure 3. Statistical properties of lunar photoelectrons observed by ARTEMIS (see text for details of the selection criteria): (a) energy spectra of upward electrons and (b) scatterplot of upward electron flux versus solar photon flux. The magenta diamond in Figure 3b indicates the data points corresponding to the Apollo measurements [Burke *et al.*, 1975]. (c) Current balance solutions of positive lunar surface potentials as a function of downward electron flux and 1–5 nm solar photon flux, calculated from equations (3) and (5) with $a = 5.0 \times 10^{-3}$ and $k = 3.5$. In Figure 3c, the vertical lines show a range of variations in 1–5 nm photon flux based on 11 year data of FISM daily spectra [Chamberlin *et al.*, 2007], whereas the horizontal lines indicate downward fluxes of isotropic Maxwellian electrons with typical densities and temperatures in the tail lobes.

we chose the photon energy range of ~ 200 – 1000 eV to represent the input photon flux relevant to ~ 100 eV photoelectron emission. Figure 3a demonstrates that the measured upward electron spectra exhibit stable, consistent shapes (approximately power law E^{-k} with $k \sim 3$ – 4) with magnitudes scaled with the 1–5 nm solar photon flux (colors). Figure 3b shows a scatterplot of the upward electron flux integrated over 80–300 eV as a function of 1–5 nm solar photon flux. We observe a good linear correlation (0.77) between the photoelectron and photon fluxes, thereby providing direct observational evidence for the modulation of lunar surface photoemission in response to solar photon flux variations. We obtain a mean photoelectron/photon flux ratio of 5.0×10^{-3} with 2 standard deviations of 1.6×10^{-3} , which bracket most of the data points (see the blue lines in Figure 3b). In Figure 3b, it is also seen that the Apollo data point from Burke *et al.* [1975] (the magenta diamond) is within the variability of ARTEMIS measurements at the corresponding photon flux.

3. An Empirical Model

We can utilize the approximately power law nature of the high-energy (>10 eV) tail photoelectron spectra and the linear dependence of the integrated photoelectron flux on the solar photon flux to develop an empirical energy distribution of the high-energy photoelectrons accounting for solar photon flux variations. First, we assume that the energy spectrum of the high-energy photoelectrons is represented by a power law distribution

$$J_e(E) = CE^{-k}, \quad (1)$$

where $k \sim 3$ – 4 based on the ARTEMIS and Apollo measurements. The comparison between the 80–300 eV photoelectron flux and the 1–5 nm photon flux suggests a linear relation

$$F_{e,80-300\text{eV}} = aF_{\gamma,1-5\text{nm}}, \quad (2)$$

where $a = (5.0 \pm 1.6) \times 10^{-3}$ representing the upper and lower brackets of the variability of the measured photoelectron/photon flux ratios (Figure 3b). From (2) and $F_{e,80-300\text{eV}} = \pi \int_{80\text{eV}}^{300\text{eV}} J_e(E)dE = \pi C(80^{-k+1} - 300^{-k+1})/(k - 1)$, we obtain

$$C = \frac{aF_{\gamma,1-5\text{nm}}(k - 1)}{\pi(80^{-k+1} - 300^{-k+1})}. \quad (3)$$

Note that J_e is in $/\text{cm}^2/\text{st}/\text{eV}$, E is in eV, and $F_{\gamma,1-5\text{nm}}$ is in $/\text{cm}^2/\text{s}$. The dotted black lines in Figure 2k show the model photoelectron spectra (1) for the FISM-derived photon flux on 29 December 2012 with parameters $a = (5.0 \pm 1.6) \times 10^{-3}$ and $k = 3.5$. The model spectra roughly reproduce the measured electron spectra (red and blue) within the uncertainty of U_M .

On the dayside lunar surface in the terrestrial tail lobes, currents from ions and secondary electrons are negligible compared to the photoelectron and ambient electron currents. Equating the downward electron flux and the upward flux of escaping photoelectrons with energies above $|eU_M|$,

$$F_{e,\text{down}} = F_{e,\text{up}} = \pi \int_{|eU_M|}^{\infty} J_e(E) dE = \frac{\pi C}{k-1} |eU_M|^{-k+1}, \quad (4)$$

we obtain a current balance solution of the lunar surface potential

$$|eU_M| = \left(\frac{k-1}{\pi C} F_{e,\text{down}} \right)^{\frac{1}{-k+1}}. \quad (5)$$

As described by this equation, the current balance surface potential (U_M) can be predicted from the input photon flux (included in C) and the input electron flux ($F_{e,\text{down}}$). Figure 3c shows the current balance solution of U_M calculated from equation (5) as a function of downward electron flux and 1–5 nm solar photon flux for parameters $a = 5.0 \times 10^{-3}$ and $k = 3.5$. The vertical lines denote ranges of 1–5 nm solar flux variations derived from 11 years of daily FISM data [Chamberlin *et al.*, 2007], whereas the horizontal lines indicate typical ranges of downward electron flux in the terrestrial magnetotail lobes. For the 29 December 2012 event, we obtain the downward electron flux, $F_{e,\text{down}} = 2.9 \times 10^7$ /cm²/s, based on a kappa function fit to the measured downward electron spectrum. The corresponding data point is shown by the black diamond in Figure 3c. This event shows the downward electron flux higher than the typical lobe fluxes because of the presence of additional cold plasma of lunar origin, which leads to decrease in the spacecraft potential (Figure 2b) [Harada *et al.*, 2013]. The predicted values of U_M for this event with $a = (5.0 \pm 1.6) \times 10^{-3}$ and $k = 3-4$ range between +22 V and +41 V, which are roughly consistent with, but slightly higher than, $U_M \sim +15-25$ V obtained from the ion reflectometry. The slight overestimation of U_M could be attributed to underestimation of the downward electron flux caused by the presence of coldest electrons which have energies lower than the instrument resolution and cannot be separated from spacecraft photoelectrons.

4. Implications

We can utilize the current balance solution (5) to estimate an enhancement of U_M induced by a solar flare. Sternovsky *et al.* [2008] estimated that dayside lunar surface potentials in the solar wind plasma vary from +5 V for the solar minimum and +7 V for the solar maximum up to +9 V during an X28 class solar flare, resulting mainly from solar photon flux variations in the 70–100 nm range. Meanwhile, the 1–5 nm solar photon flux can increase by a factor of 10 or more during an X-class flare [Chamberlin *et al.*, 2008]. As an example, multiplying $F_{\gamma,1-5\text{nm}}$ by 10 for the 2012-12-29 event results in a factor of $\sim 2-3$ increase in U_M , ranging from +70 V to +98 V. In Figure 3c, we can see that a factor of 10 increase in 1–5 nm photon flux with the same downward electron flux (an order of magnitude horizontal shift toward the right) generally results in a factor of a few increase in U_M (colors). The current balance solution suggests that lunar surface charging in the tail lobes could enhance substantially and reach very large potentials (on the order of +100 V) during strong solar flares.

In this paper, we have focused on photoemission and charging on the unmagnetized regions of the lunar surface. As Burke *et al.* [1975] suggested, even larger potentials could exist on the lunar surface with strong crustal magnetic fields because of charge separation electric fields. Further investigation on plasma processes above the photoemitting, magnetized surface would be necessary to fully characterize both spatial and temporal variabilities of lunar surface potentials.

An accurate understanding of the emitted photoelectron spectrum from lunar soil is critical for understanding the charging and transport mechanisms of lunar dust that have been theorized for the Moon and asteroids [Veverka *et al.*, 2001; Colwell *et al.*, 2005; Poppe *et al.*, 2012b]. Recent laboratory and simulation efforts have shown that grain-scale “supercharging” may be responsible for electrostatic ejection and transport of individual grains [Wang *et al.*, 2016; Zimmerman *et al.*, 2016]. The high-energy ($\sim 20-300$ eV) photoelectron spectrum measured by ARTEMIS from the lunar soil should be incorporated into on-going modeling and theoretical efforts in order to fully understand electrostatic charging, mobilization, and bulk transport of dust grains on airless bodies.

Acknowledgments

The authors acknowledge support through NASA contract NAS5-02099, as well as V. Angelopoulos for use of data from the THEMIS mission, J. W. Bonnell and F. S. Mozer for use of EFI data, and K. H. Glassmeier, U. Auster, and W. Baumjohann for use of FGM data, provided under the lead of the Technical University of Braunschweig (Germany) and with financial support from both the German Ministry for the Economy and Technology and the German Center for Aviation and Space (DLR) under contract 50 OC 0302. ARTEMIS data are publicly available at <http://artemis.ssl.berkeley.edu>. FISM data are publicly available at <http://lasp.colorado.edu/lisird/fism>.

References

- Angelopoulos, V. (2011), The ARTEMIS mission, *Space Sci. Rev.*, *165*(1–4), 3–25, doi:10.1007/s11214-010-9687-2.
- Auster, H. U., et al. (2008), The THEMIS fluxgate magnetometer, *Space Sci. Rev.*, *141*(1–4), 235–264, doi:10.1007/s11214-008-9365-9.
- Bonnell, J. W., F. S. Mozer, G. T. Delory, A. J. Hull, R. E. Ergun, C. M. Cully, V. Angelopoulos, and P. R. Harvey (2008), The Electric Field Instrument (EFI) for THEMIS, *Space Sci. Rev.*, *141*(1–4), 303–341, doi:10.1007/s11214-008-9469-2.
- Burke, W. J., P. H. Reiff, and D. L. Reasoner (1975), The effect of local magnetic fields on the lunar photoelectron layer while the moon is in the plasma sheet, paper presented at 6th Lunar Science Conference, pp. 2985–2997, Houston, Tex., 17–21 Mar.
- Chamberlin, P. C., T. N. Woods, and F. G. Eparvier (2007), Flare Irradiance Spectral Model (FISM): Daily component algorithms and results, *Space Weather*, *5*, S07005, doi:10.1029/2007SW000316.
- Chamberlin, P. C., T. N. Woods, and F. G. Eparvier (2008), Flare Irradiance Spectral Model (FISM): Flare component algorithms and results, *Space Weather*, *6*, S05001, doi:10.1029/2007SW000372.
- Colwell, J. E., A. A. Gulbis, M. Horányi, and S. Robertson (2005), Dust transport in photoelectron layers and the formation of dust ponds on Eros, *Icarus*, *175*(1), 159–169, doi:10.1016/j.icarus.2004.11.001.
- Goldstein, B. E. (1974), Observations of electrons at the lunar surface, *J. Geophys. Res.*, *79*(1), 23–35, doi:10.1029/JA079i001p00023.
- Halekas, J. S., D. L. Mitchell, R. P. Lin, S. Frey, L. L. Hood, M. H. Acuña, and A. B. Binder (2001), Mapping of crustal magnetic anomalies on the lunar near side by the Lunar Prospector electron reflectometer, *J. Geophys. Res.*, *106*, 27,841–27,852, doi:10.1029/2000JE001380.
- Harada, Y., S. Machida, J. S. Halekas, A. R. Poppe, and J. P. McFadden (2013), ARTEMIS observations of lunar dayside plasma in the terrestrial magnetotail lobe, *J. Geophys. Res. Space Physics*, *118*, 3042–3054, doi:10.1002/jgra.50296.
- Henke, B. L., J. A. Smith, and D. T. Attwood (1977), 0.1–10-keV X-ray-induced electron emissions from solids—models and secondary electron measurements, *J. Appl. Phys.*, *48*(5), 1852–1866, doi:10.1063/1.323938.
- Henke, B. L., J. P. Knauer, and K. Premaratne (1981), The characterization of X-ray photocathodes in the 0.1–10-keV photon energy region, *J. Appl. Phys.*, *52*(3), 1509–1520, doi:10.1063/1.329789.
- Lin, R. P., and R. Gopalan (1991), Mapping the composition of planetary surfaces by Auger electron spectroscopy, *Rev. Sci. Instrum.*, *62*(3), 660–666, doi:10.1063/1.1142064.
- Manka, R. (1973), Plasma and potential at the lunar surface, *Astrophys. Space Sci.*, *37*, 347–361, doi:10.1007/978-94-010-2647-5_22.
- McFadden, J. P., C. W. Carlson, D. Larson, M. Ludlam, R. Abiad, B. Elliott, P. Turin, M. Marckwordt, and V. Angelopoulos (2008), The THEMIS ESA plasma instrument and in-flight calibration, *Space Sci. Rev.*, *141*(1–4), 277–302, doi:10.1007/s11214-008-9440-2.
- Mitchell, D. L., J. S. Halekas, R. P. Lin, S. Frey, L. L. Hood, M. H. Acuña, and A. B. Binder (2008), Global mapping of lunar crustal magnetic fields by lunar prospector, *Icarus*, *194*, 401–409, doi:10.1016/j.icarus.2007.10.027.
- Pedersen, A. (1995), Solar wind and magnetosphere plasma diagnostics by spacecraft electrostatic potential measurements, *Ann. Geophys.*, *13*(2), 118–129, doi:10.1007/s00585-995-0118-8.
- Poppe, A. R., R. Samad, J. S. Halekas, M. Sarantos, G. T. Delory, W. M. Farrell, V. Angelopoulos, and J. P. McFadden (2012a), ARTEMIS observations of lunar pick-up ions in the terrestrial magnetotail lobes, *Geophys. Res. Lett.*, *39*, L17104, doi:10.1029/2012GL052909.
- Poppe, A. R., M. Piquette, A. Likhanskii, and M. Horányi (2012b), The effect of surface topography on the lunar photoelectron sheath and electrostatic dust transport, *Icarus*, *221*(1), 135–146, doi:10.1016/j.icarus.2012.07.018.
- Poppe, A. R., J. S. Halekas, R. Samad, M. Sarantos, and G. T. Delory (2013), Model-based constraints on the lunar exosphere derived from ARTEMIS pickup ion observations in the terrestrial magnetotail, *J. Geophys. Res. Planets*, *118*, 1135–1147, doi:10.1002/jgre.20090.
- Reasoner, D. L., and W. J. Burke (1973), Measurement of the lunar photoelectron layer in the geomagnetic tail, *Astrophys. Space Sci.*, *37*, 369–387, doi:10.1007/978-94-010-2647-5_24.
- Sternovsky, Z., P. Chamberlin, M. Horanyi, S. Robertson, and X. Wang (2008), Variability of the lunar photoelectron sheath and dust mobility due to solar activity, *J. Geophys. Res.*, *113*, A10104, doi:10.1029/2008JA013487.
- Stubbs, T., R. Vondrak, and W. Farrell (2006), A dynamic fountain model for lunar dust, *Adv. Space Res.*, *37*(1), 59–66, doi:10.1016/j.asr.2005.04.048.
- Tanaka, T., et al. (2009), First in situ observation of the Moon-originating ions in the Earth's Magnetosphere by MAP-PACE on SELENE (KAGUYA), *Geophys. Res. Lett.*, *36*, L22106, doi:10.1029/2009GL040682.
- Tsunakawa, H., F. Takahashi, H. Shimizu, H. Shibuya, and M. Matsushima (2015), Surface vector mapping of magnetic anomalies over the Moon using Kaguya and Lunar Prospector observations, *J. Geophys. Res. Planets*, *120*, 1160–1185, doi:10.1002/2014JE004785.
- Vasyliunas, V. (1968), A survey of low-energy electrons in the evening sector of the magnetosphere with OGO 1 and OGO 3, *J. Geophys. Res.*, *73*(9), 2839–2884, doi:10.1029/JA073i009p02839.
- Veverka, J., et al. (2001), Imaging of small-scale features on 433 Eros from NEAR: Evidence for a complex regolith, *Science*, *292*(5516), 484–488, doi:10.1126/science.1058651.
- Wang, X., J. Schwan, H.-W. Hsu, E. Grün, and M. Horányi (2016), Dust charging and transport on airless planetary bodies, *Geophys. Res. Lett.*, *43*, 6103–6110, doi:10.1002/2016GL069491.
- Whipple, E. C. (1981), Potentials of surfaces in space, *Rep. Prog. Phys.*, *44*(11), 1197–1250, doi:10.1088/0034-4885/44/11/002.
- Winslow, R. M., et al. (2014), Mercury's surface magnetic field determined from proton-reflection magnetometry, *Geophys. Res. Lett.*, *41*, 4463–4470, doi:10.1002/2014GL060258.
- Zimmerman, M. I., W. M. Farrell, C. M. Hartzell, X. Wang, M. Horanyi, D. M. Hurlley, and K. Hibbitts (2016), Grain-scale supercharging and breakdown on airless regoliths, *J. Geophys. Res. Planets*, *121*, 2150–2165, doi:10.1002/2016JE005049.